Supplementary Materials

Thermally triggered shape-memory polyimide composite aerogels for strain-locked electromagnetic wave absorption

Lu Yang[1,#], Huiya Wang[1,#], Zhao Yang[1], Chen Qian[1], Innocent Toendepi[1], Tian Mai[1], Qixin Yang[2,*], Yaofeng Zhu[1,*]

[1]School of Materials Science and Engineering, Zhejiang Sci-Tech University, Hangzhou 310018, Zhejiang, China.
[2]School of Biological and Chemical Engineering, Zhejiang University of Science and Technology, Hangzhou 310023, Zhejiang, China.
[#]These authors contributed equally to this work.

[*]**Correspondence to:** Prof. Yaofeng Zhu, School of Materials Science and Engineering, Zhejiang Sci-Tech University, Hangzhou 310018, Zhejiang, China. E-mail: yfzhu@zstu.edu.cn; Dr. Qixin Yang, School of Biological and Chemical Engineering, Zhejiang University of Science and Technology, Hangzhou 310023, Zhejiang, China. E-mail: qixinyang@zust.edu.cn

1 Experimental section

1.1 The synthesis strategy of reduced graphene oxide:

It should be noted that rGO was not prepared separately. GO was thermally reduced in situ during the imidization process, resulting in the formation of the conductive rGO framework within the composite aerogel.

1.2 Data analysis

All data visualization was performed using OriginPro 2022(OriginLab, Northampton, MA, USA). Schematic illustrations were created using Microsoft PowerPoint (Microsoft, Redmond, WA, USA), and aerogel structures were rendered with Blender 4.5(Blender Foundation, Amsterdam, The Netherlands).

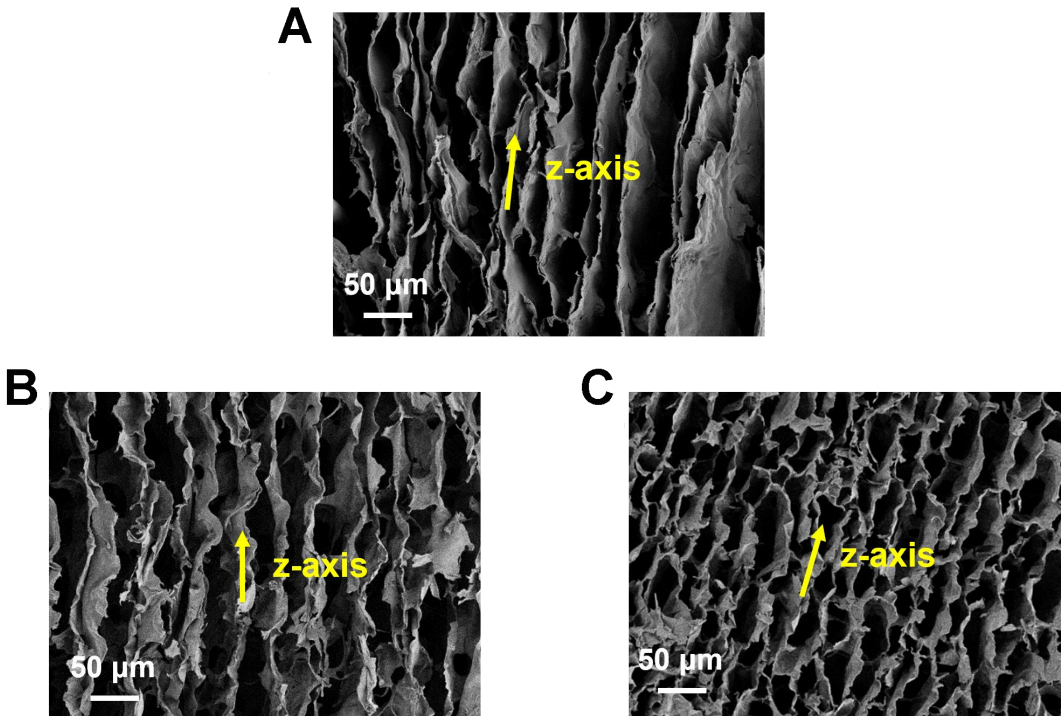

Supplementary Figure 1. SEM images of (A) PGAA-0, (B) PGAA-1, and (C) PGAA-3.

According to the transmission line theory, reflection loss (*RL*) is a reliable approach to evaluate electromagnetic absorption performance, which can be calculated by the following formula:

$$Z = \left|\frac{Z_{in}}{Z_0}\right| = \sqrt{\frac{\mu_r}{\varepsilon_r}} \tanh\left(\frac{j2\pi fd}{c}\sqrt{\mu_r \varepsilon_r}\right) \quad (1)$$

$$RL = 20\log\left|\frac{Z_{in} - Z_0}{Z_{in} + Z_0}\right| \quad (2)$$

where Z_{in}, Z_0, μ_r and ε_r are the input impedance of absorber, free space impedance, complex permeability and complex permittivity, respectively. f, d, and c represent frequency, thickness, and velocity of light. Generally, the *RL* value less than 10 dB accounts for 90% of the absorbed electromagnetic wave, and the corresponding frequency band is referred to as EAB.

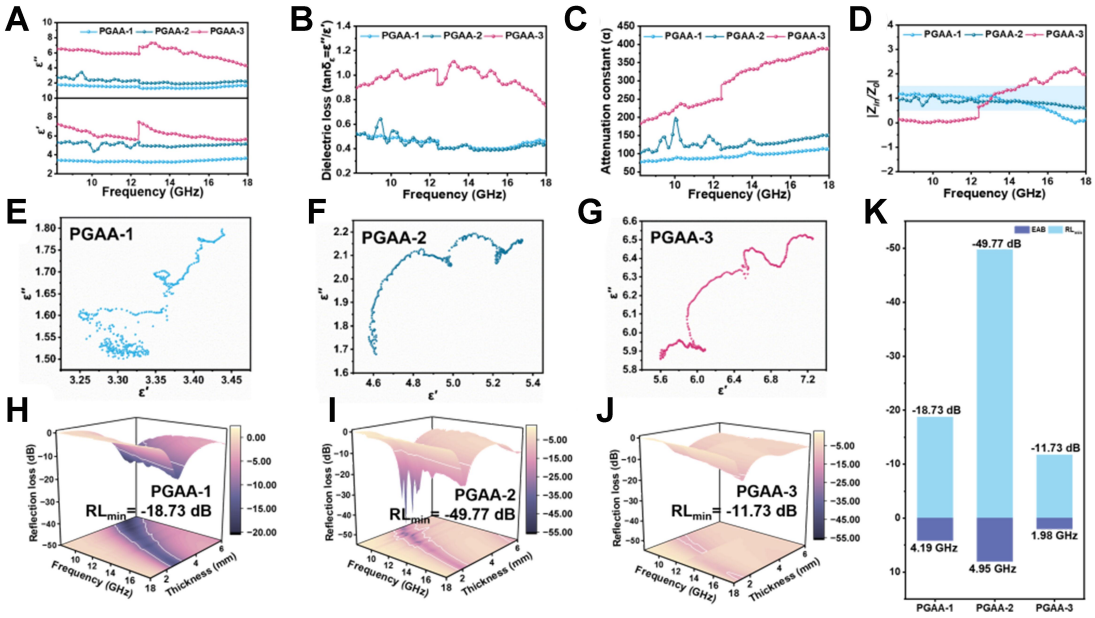

Supplementary Figure 2. (A) ε′ and ε″, (B) tanδε, (C) α, (D) $|Z_{in}/Z_0|$, (E-G) Cole-cole curves, (H-J) 3D reflection loss curves, (K) Comparison chart of EAB and RL_{min} of PGAA-1, PGAA-2, and PGAA-3.

Compression strain experiments

To investigate the strain-dependent properties, PGAA and PGAA-PTA composite aerogels were subjected to two different compression protocols. The resulting samples were denoted as PGAA-X and PGAA-PTA-X, where X represents the target compressive strain of 20%, 40%, or 60%.

For PGAA aerogels, a continuous external-force compression method was employed. The samples were compressed to the target strain, and the external load was maintained throughout subsequent measurements to preserve the prescribed deformation state.

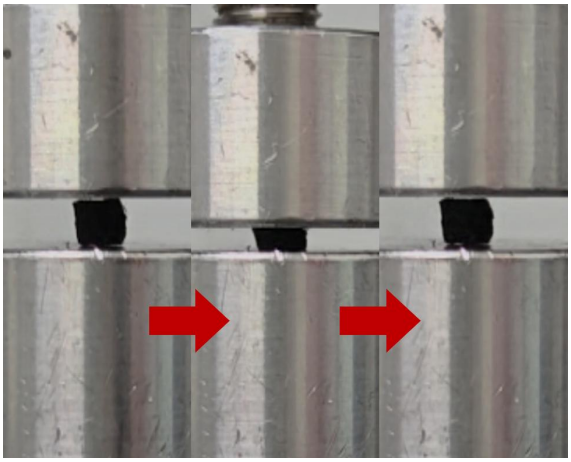

Supplementary Figure 3. The mechanical compression and release process of PGAA aerogel.

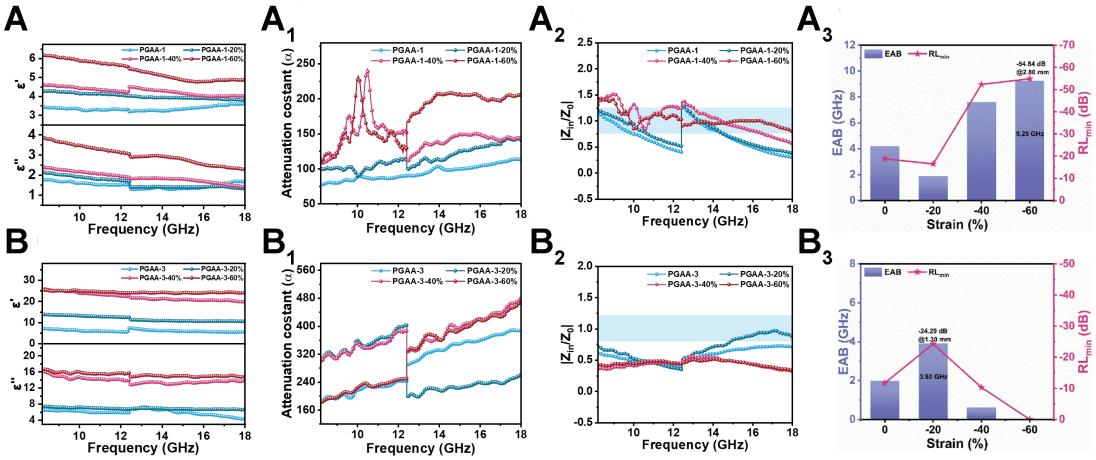

Supplementary Figure 4. Electromagnetic and microwave absorption properties of PGAA under different compressive strains: ε′, ε″, $|Z_{in}/Z_0|$, α and RL_{min} and EAB values for (A-A_3) PGAA-1 and (B-B_3) PGAA-3.

The shape-fixity ratio (R_f) and shape-recovery ratio (R_r) are defined from the one-way thermomechanical DMA cycle as:

$$R_f=(\varepsilon_f/\varepsilon_m)\times 100\% \quad (3)$$

$$R_r=[(\varepsilon_m-\varepsilon_r)/\varepsilon_m]\times 100\% \quad (4)$$

where ε_m is the maximum programmed compressive strain, ε_f is the strain retained after unloading in the cooled state, and ε_r is the residual strain after free recovery. These follow the standard one-way shape-memory protocol for shape-memory polymers and aerogels. We have also clarified that ε_f is read after removal of the external load.

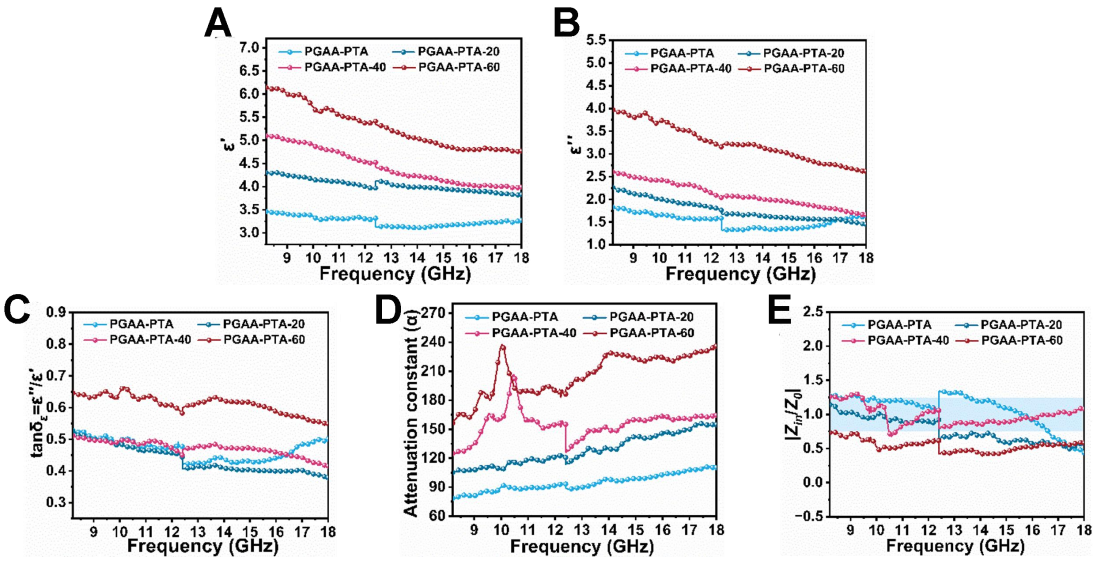

Supplementary Figure 5. (A) ε′, (B) ε′, (C) $\tan\delta_\varepsilon$, (D) α, and (E) $|Z_{in}/Z_0|$ of PGAA-PTA at different compressive strains.

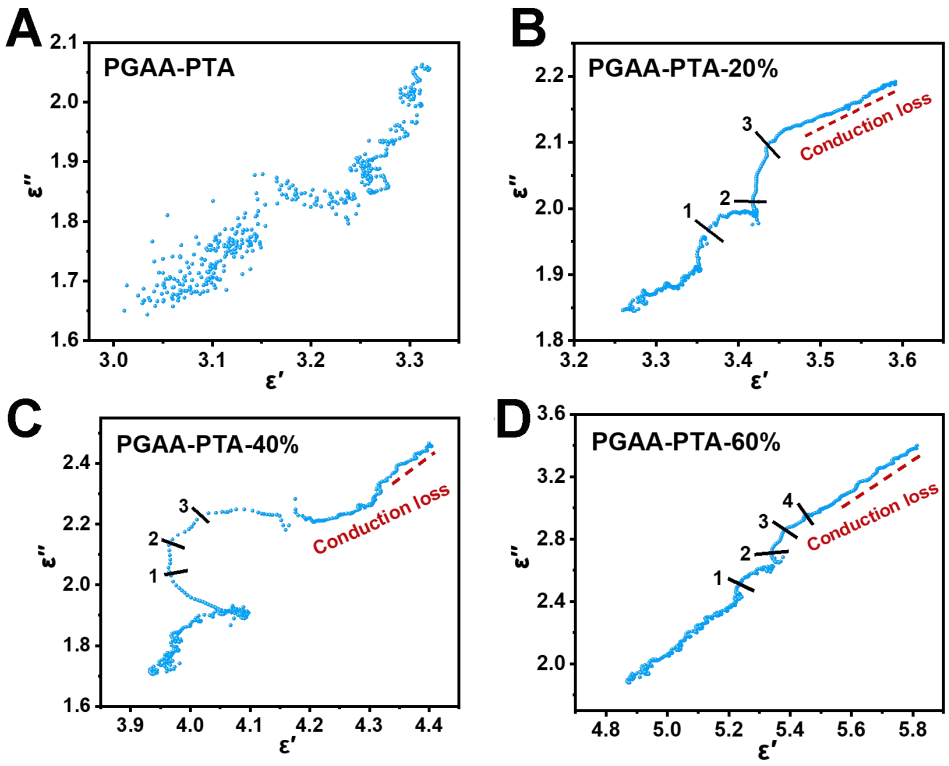

Supplementary Figure 6. (A-D) Cole-Cole curves of PGAA-PTA at different compressive strains.

According to the Debye relaxation model with conductivity correction, the total dielectric loss can be separated into polarization and conduction components, as expressed in the following formula:

$$\varepsilon_c'' = \frac{\delta}{\omega\varepsilon_0} \tag{5}$$

$$\varepsilon_p'' = \frac{\varepsilon_s - \varepsilon_\infty}{1+\omega 2\tau 2}\omega\tau \tag{6}$$

$$\varepsilon'' = \frac{\varepsilon_s - \varepsilon_\infty}{1+\omega 2\tau 2}\omega\tau + \frac{\delta}{\omega\varepsilon_0} = \varepsilon_p'' + \varepsilon_c'' \tag{7}$$

where ε_p'' represents the polarization loss part in the dielectric loss, ε_c'' represents the conductivity loss part, and ε_0 is the vacuum permittivity. τ is the relaxation time, δ represents the conductivity of the material. As shown in Figure S7a, the polarization-to-conduction loss ratio remains greater than unity over the entire investigated frequency range for all locked strains, indicating that polarization loss is the predominant dielectric-loss component. This behavior is consistent with the abundant heterogeneous interfaces and polar groups in the PGAA-PTA aerogel. Both polarization and conduction losses increase progressively with compressive strain (Figure S7 b,c), owing to the reduced separation between conductive frameworks, increased interfacial contact, and enhanced connectivity of the conductive network. Notably, the relative contribution of conduction loss becomes more pronounced after compression, particularly in the Ku band, leading to a lower polarization-to-conduction loss ratio than that of the uncompressed aerogel. These results indicate that compression shifts the dielectric dissipation from strongly polarization-dominated behavior toward a more balanced cooperation between polarization and conduction losses. The optimum absorption at 40% strain, however, arises from the combined balance between dielectric attenuation and impedance matching rather than from the maximum loss magnitude alone.

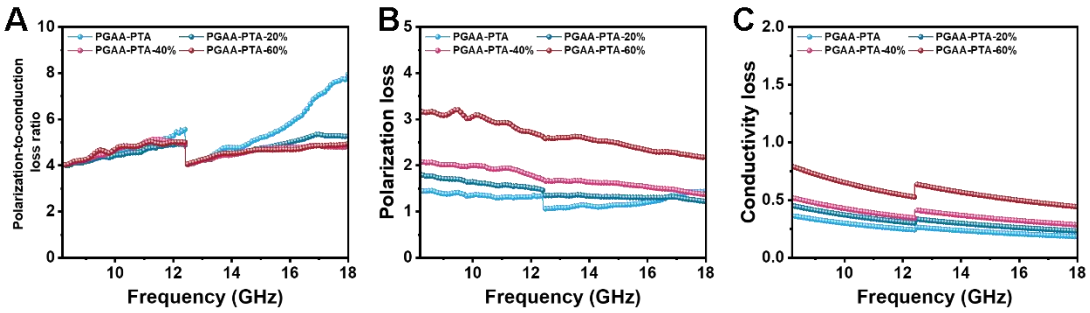

Supplementary Figure 7. Frequency dependence of (A) the polarization-to-conduction loss ratio (B) polarization loss (C) conduction loss for PGAA-PTA at different compressive strains.

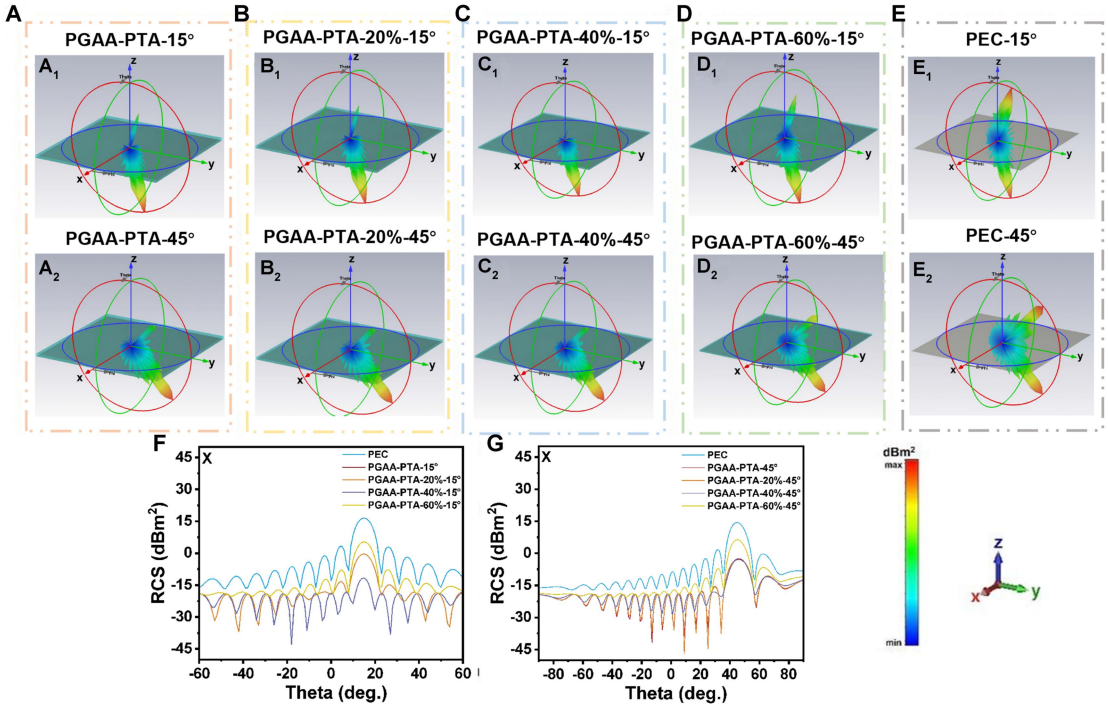

Supplementary Figure 8. Simulated far-field scattering responses of PGAA–PTA aerogels under oblique incidence at 9.5 GHz. Three-dimensional scattering patterns of PGAA–PTA aerogels at compression strains of (A) 0%, (B) 20%, (C) 40%, and (D) 60%, together with (E) the PEC reference, under incident angles of 15° (A_1–E_1) and 45° (A_2–E_2). Corresponding angular RCS profiles in the θ direction at incident angles of (F) 15° and (G) 45°

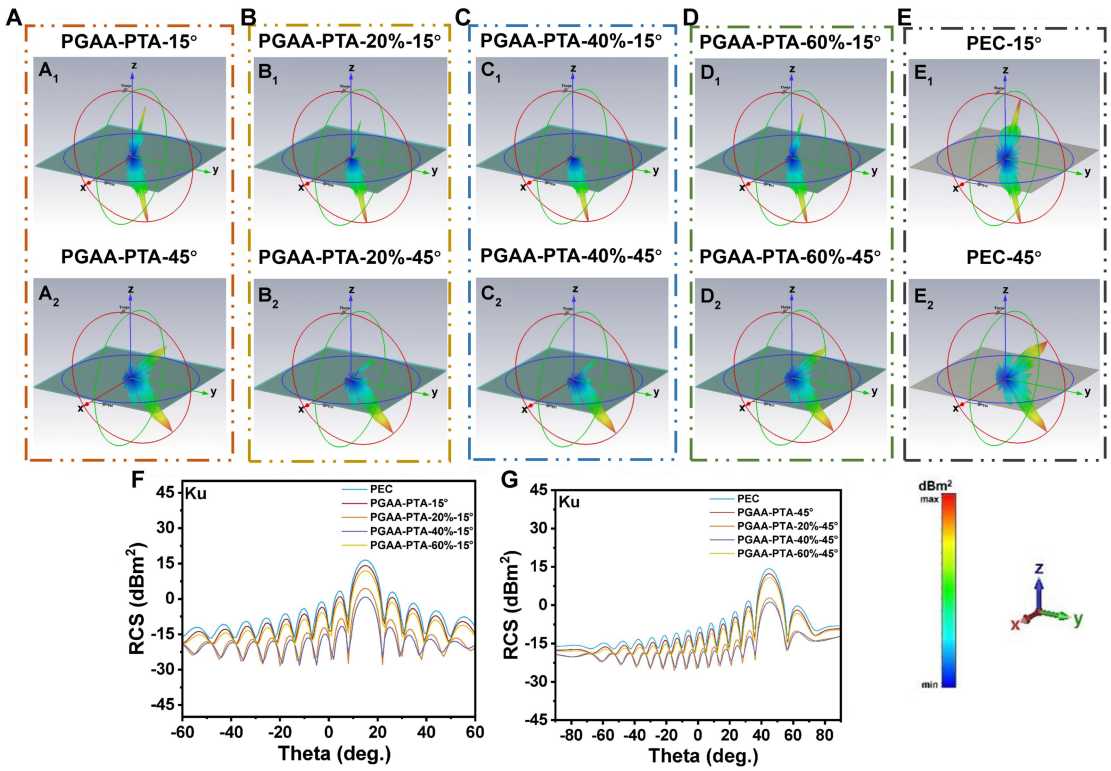

Supplementary Figure 9. Simulated far-field scattering responses of PGAA–PTA aerogels under oblique incidence in the Ku band. Three-dimensional scattering patterns of PGAA–PTA aerogels at compression strains of (A) 0%, (B) 20%, (C) 40%, and (D) 60%, together with (E) the PEC reference, at incident angles of 15° (A_1–E_1) and 45° (A_2–E_2). Corresponding angular RCS profiles in the θ direction at incident angles of (F) 15° and (G) 45°.

The full-wave simulations were performed in CST Studio Suite. The experimentally measured electromagnetic parameters of the PGAA-PTA foams under 0%, 20%, 40%, and 60% compression strains were used as the material inputs. A perfect electric conductor (PEC) plate with dimensions of 225 mm × 225 mm × 0.1 mm was used as the reference model, and a linearly polarized plane electromagnetic wave was used as the excitation source, with frequencies of 9.5 GHz and 12.5 GHz adopted for the X-band and Ku-band conditions, respectively.

The simulation was governed by Maxwell's equations:

$$\nabla \times E = -j\omega\mu H \tag{8}$$

$$\nabla \times H = j\omega\varepsilon E + \sigma E \tag{9}$$

where E and H are the electric and magnetic fields, ω is the angular frequency, ε is the permittivity, μ is the permeability, and σ is the electrical conductivity. The radar cross section was calculated according to:

$$\sigma_{RCS} = \lim_{r\to\infty} 4\pi r^2 \frac{|E_s|^2}{|E_i|^2} \tag{10}$$

$$RCS = 10\log_{10}(\delta_{RCS}) \tag{11}$$

where E_s and E_i represent the scattered and incident electric fields, respectively.

In addition, a linearly polarized plane wave was used. The oblique incidence was introduced by changing the propagation direction of the incident wave. For an incident angle of θ, the propagation vector was set as:

$$k = (0, sin\theta, -cos\theta) \tag{12}$$

and the electric field vector was kept as:

$$E = (1,0,0) \tag{13}$$

Thus, the electric field remained perpendicular to the propagation direction. Incident angles of 15° and 45° were considered. The far-field scattering behavior was then analyzed by three-dimensional scattering patterns, two-dimensional polar plots, angular RCS profiles, and average RCS values over the theta range from -90° to 90°.

Supplementary Table 1. performances contrast

Materials	condition	RL_{min} (dB)	EAB (GHz)	d (mm)	
$Ti_3C_2T_x$/ ANF/PI aerogel	Temperature: 25 °C	-21.58	2.40	2.10	[1]
	Temperature: 200 °C	-46.24	2.96	1.90	
GO aerogel	Compression: 0%	-16.59	3.16	6.87	[2]
	Compression: 30%	61.09	6.30	4.81	
CNTs/CNF-WPU aerogel	Compression: 10%	-15.20	/	6.60	[3]
	Compression: 40%	-67.20	≥4.2 GHz	4.60	
CNTs/$Ti_3C_2T_x$-WPU aerogel	Compression: 0%	-18.90	1.80	4.80	[4]
	Compression: 42%	-68.30	3.20	2.80	
rGO/SiC/ $CoFe_2O_4$ composites	/	-62.39	1.40	2.43	[5]
ANF/rGO /PI composite aerogels	/	-41.0	4.20	5.1-6.9	[6]
BC/ rGO aerogel	/	-38.52	6.68	3.50	[7]
PIC/rGO	/	-57.22	3.12	4.36	[8]
PGAA-PTA	Compression: 0%	-19.17	2.33	5.10	This work
	Compression: 40%	-72.95	7.11	3.20	

REFERENCES

[1] Yang F.; Yao J.; Jin L.; et al. Multifunctional $Ti_3C_2T_x$ MXene/aramid nanofiber/polyimide aerogels with efficient thermal insulation and tunable electromagnetic wave absorption performance under thermal environment, *Composites Part B: Engineering* **2022**, *243*, 110161. DOI: 10.1016/j.compositesb.2022.110161.

[2] Wang Z.; Wei R.; Gu J.; et al. Ultralight, highly compressible and fire-retardant graphene aerogel with self-adjustable electromagnetic wave absorption, Carbon 2018, 139, 1126-1135. doi: 10.1016/j.carbon.2018.08.014.

[3] Kong L.; Zhang S.; Liu Y.; et al. Flexible CNTs/CNF-WPU aerogel for smart electromagnetic wave absorbing with tuning effective absorption bandwidth, *Carbon* **2023**, *207*, 13-22. doi:10.1016/j.carbon.2023.02.067.

[4] Kong L.; Zhang G.; Cui H.; et al. Deformation induced absorption band-tunable smart CNTs/$Ti_3C_2T_x$-WPU electromagnetic wave absorbing aerogel, *Carbon* **2024**, *223*, 119023. doi:10.1016/j.carbon.2024.119023.

[5] Wang J.; Hu S.; Tang Q.; et al. One-pot hydrothermally prepared RGO/SiC/$CoFe_2O_4$ composites with strong microwave absorption at different thicknesses, *Ceramics International* **2022**, *48*(20), 30640-30650. doi:10.1016/j.ceramint.2022.07.007.

[6] Zhou Y.; Wang S. j.; Li D. S.; et al. Lightweight and recoverable ANF/rGO/PI composite aerogels for broad and high-performance microwave absorption, *Composites Part B: Engineering* **2021**, *213*, 108701. doi:10.1016/j.compositesb.2021.108701.

[7] Zhang Y.; Wang J.; Wu Q.; et al. Enhanced electromagnetic wave absorption of bacterial cellulose/reduced graphene oxide aerogel by eco-friendly in-situ construction, *Journal of Colloid and Interface Science* **2025**, *678*, 648-655. doi:10.1016/j.jcis.2024.08.211.

[8] Wang Z.; Min Y.; Fang J.; et al. Polyimide aerogel-derived amorphous porous carbon/crystalline carbon composites for high-performance microwave absorption, *RSC Advances* **2023**, *13*(11), 7055-7062. doi:10.1039/D3RA00155E.